Transient-based fault identication algorithm using parametric models for meshed HVDC grids

P. Verrax, A. Bertinato, Michel Kieffer, B. Raison

Transient-based fault identification algorithm using parametric models for meshed HVDC grids

P. Verrax[a,b,*], A. Bertinato[a], M. Kieffer[a,b], B. Raison[a,c]

[a] SuperGrid Institute, 23 rue Cyprian, BP 1321, 69611 Villeurbanne Cedex, France
[b] L2S, Univ Paris-Sud, CNRS, CentraleSupelec, Univ Paris-Saclay, Gif-sur-Yvette F-91190, France
[c] Univ. Grenoble Alpes, CNRS, Grenoble INP*, G2Elab, 38000 Grenoble, France. (* Institute of Engineering Univ. Grenoble Alpes)

Abstract

This paper addresses the problem of fault identification in meshed HVDC grids once an abnormal behavior has been detected. A parametric single-ended fault identification algorithm is proposed. The method is able to determine whether the line monitored by a relay is faulty or not using a very short observation window. When a fault is suspected, the proposed algorithm estimates the fault distance and impedance using a parametric model describing the voltage and current evolution just after the fault occurrence. This model combines physical and behavioral parts to represent the fault propagation and to account for ground effects and various losses. The identification of the faulty line is then based on the size of the confidence region of the obtained estimate. The performance of the algorithm for a three-node meshed grid is studied using Electro-Magnetic Transient (EMT) simulations. On the considered grid model, the current and voltage need to be observed during less than 0.2ms to get a sufficiently accurate estimate of the fault characteristics and identify consistently the faulty line.

Keywords: HVDC, Multi-terminal, protection, fault detection, fault localization, parameter identification

1. Introduction

In the future, Multi-Terminal high-voltage Direct-Current (MTDC) grids are likely to act as a backbone to the existing AC network, providing better interconnection over large distances between renewable energy sources and consumption area as well as integration of large offshore wind power plants [1]. Among the several technical and non-technical barriers still to overcome for the development of High-Voltage Direct-Current (HVDC) meshed grids, the protection of the lines is seen as one of the most challenging [2]. Protection strategies and breaker technologies developed in the case of High Voltage Alternative Current (HVAC) grids cannot be directly translated to HVDC grids, since, for example, faults on an HVDC line, do not lead to a zero-crossing of the current, which makes the fault clearance more difficult.

The main tasks of a protection strategy include fault detection, faulty component identification, and tripping of the breakers, see [3]. If the breakers are triggered before the faulty component is identified, so that a large part of the grid is de-energized, one refers to as a non-selective fault clearing strategy, see for instance [4]. On the opposite, selective fault clearing strategies consist in identifying the faulty component so that only the corresponding breakers are triggered, which is considered preferable since this minimizes the impact of the fault on the grid. In such a strategy, breaking modules located at the end of each line are responsible for the protection of their respective line, see Figure 1. Overall, protection strategies must be reliable [5], *i.e.*, they must lead to an isolation of the protected line only when needed and must be immune to changes caused by normal operations on the grid. Finally, protection algorithms must operate fast enough to cope with Direct Current Circuit Breaker (DCCB) capabilities. DC inductances located between each relay and the busbar are generally considered in the literature to slow down the rise of the current. In grids involving overhead lines, however, the inductive behavior of the lines may enable to omit such inductances, which is considered preferable regarding the cost and dynamic behavior of the grid [6]. Such an approach requires fast fault identification as well as fast breakers. The use of hybrid DCCB is seen as an advantageous compromise between the operating time and the breaking capabilities of the breakers, see [7]. The typical available time to detect and identify the fault is then less than a millisecond. This makes use of communication between distant protection devices not suitable, since such communications induces several milliseconds of delay, as shown in [8]. Hence, a selective protection scheme requires a single-ended (non-unit) algorithm [3] ensuring selectivity, *i.e.*, able to discriminate between internal faults, occurring on the protected line and external faults, occur-

*Corresponding author
Email address: paul.verrax@supergrid-institute.com (P. Verrax)

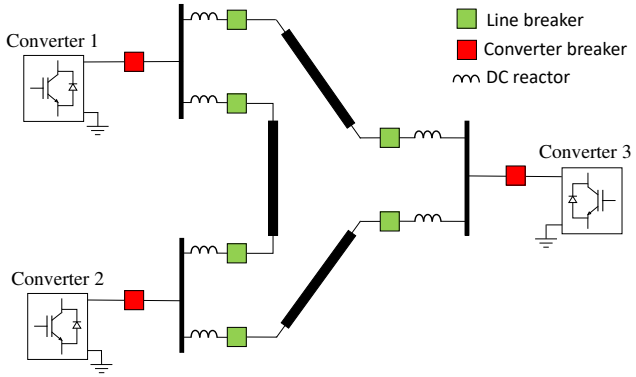

Figure 1: Example of a three-node MTDC network; DC reactors are assumed available in most state-of-the-art fault identification algorithms, whereas in the proposed approach they are not required to achieve selective fault identification.

ring elsewhere in the grid.

This paper, introduces a protection algorithm to be used in a primary selective strategy[1]. We propose a novel single ended protection algorithm able to detect and identify faults occurring on transmission lines. Each relay embeds an analytical parametric model of the evolution of the current and voltage after the occurrence of a fault, depending on a set of physical fault parameters. When a fault is suspected, an iterative maximum-likelihood (ML) estimate of the fault parameters is evaluated from the measurements available at the relay. The estimated fault parameters and their confidence intervals are exploited to determine whether or not a fault actually occurred on the protected line. Off-line transient simulations in EMTP-RV [10, 11] show that the proposed algorithm can identify most of internal faults from measurements collected over a time window of less than 0.2 ms after the detection of an abnormal behavior on the line and is immune to faults on neighboring lines. Contrary to most existing approaches, extra inductances are not required to distinguish between faults occurring on the protected line and elsewhere.

Section 2 provides an overview of existing protection algorithms. Section 3 presents the problem formulation and the proposed approach. The modeling of the fault behavior is detailed in Section 4 and the estimation algorithm for the fault parameters is described in Section 5. The identification process using confidence intervals is detailed in Section 6. Simulation results are presented in Section 7, before drawing some conclusions and future research directions in Section 8.

2. Related work

This section overviews existing detection, identification, and localization methods, focusing on single-ended algorithms. More extensive reviews of protection schemes and existing technologies can be found in [12], [13], and [14].

2.1. Amplitude-based methods

Fault behavior is generally associated with high variation rates in both current and voltage. Various methods using thresholds on voltage and/or current derivatives have been proposed.

A general method to tune such thresholds is developed in [15] using a reduced grid model instead of extensive transient response simulations. In [16], the rate of change of voltage across the DC reactors is used to detect and identify the fault. The Multi Modular Converters (MMC) arm inductances, along with large DC reactors (200 mH), are used to tune the detection thresholds.

Regarding current-based algorithm, [17] proposed a three-stage method, first detecting peaks in the deviation of the current from a moving average, then comparing the current value with previous highest values and finally comparing the current deviation to a predetermined threshold to ensure selectivity. Methods based on voltage and current derivative along with over-current methods are compared in [18], which shows that a combined criterion could achieve selective fault detection. A criterion combining the voltage and current derivatives, as well as the current second-order derivative is proposed in [19]. Additionally, the concept of critical fault resistance is used to detect only faults that would lead to current rise higher than 2 p.u.

The aforementioned algorithms share the assumption of the presence of rather large inductances at the end of each line, see Figure 1, generally required to limit the rise of current and achieve selectivity. Nevertheless, such inductances are costly and may deteriorate the dynamic performance of the system and cause instability [6]. Moreover, such methods rely on critical thresholds to ensure both dependability and selectivity.

2.2. Model-based methods

Different techniques have tried to benefit from more accurate traveling wave models describing the evolution of current and voltage when a fault appears in a line.

In [20], the S-transform of the voltage is used to detect the arrival times of the traveling waves. Along with the polarities of the waves, this allows oneto locate the fault on a given line. In a similar fashion, but in the context of AC transmission, [21] uses multiple traveling wave arrival times to spot the pattern of the reflections between the observation point and the fault. The method is then able to locate a fault on a line inserted in a meshed grid. Several traveling wave arrival times (about a dozen) need to be acquired, which limits the speed of the method. In those two methods, the key challenges consist in being able to spot accurately the wave fronts, and in being able to distinguish waves due to reflection at the fault from waves due to other reflections in the grid. Note that both algorithms also assume that the fault has already been detected on a specific line and focus on the fault accurate localization.

[1] In case of fault identification failure, a non-selective strategy such as presented in [9] can be applied as back up.

In [22], the Bergeron method is applied to reconstruct the distribution of the voltage along a healthy line using voltage and current measurements at the end of the line. The computed voltage distribution at both ends are hence correct up to the point where the line is faulty. Assuming synchronized communication is available between the relays, the fault location can be computed as the point where the reconstructed voltage from both sides are matching. Such a point can be found using a least-squares algorithm. Still using synchronized data, [23] developed a dynamic state estimation algorithm for fault localization in AC systems. A chi-square confidence test is employed to validate the results of the fault location estimation. Nevertheless, as mentioned earlier, the use of communications, especially to get synchronized data, is not suitable for fast fault detection due to measurement transmission delays, see for instance [8].

The concept of electromagnetic time reversal, used in [24], takes advantage of the time reversal invariance of electromagnetic equations such as the telegraph equations. By comparing, in reversed time, the recorded voltage at a station and a simulated voltage transient at a given observation point, one can estimate the fault location. Nevertheless, the method is meant as a localization algorithm and assumes information on the fault type from the breakers is available as well as more than 5 ms long measurement window.

When the system is based on voltage source converters with large shunt capacitance, [25] showed that this capacitance could be accurately identified in the case of internal faults using local voltage and current measurements. On the contrary, external faults would lead to an erroneous identification. In [26], a rational approximation of the characteristic admittance of the line is used to detect the first incident wave of the current. Selective detection is then achieved using a predetermined static threshold on the incident wave, still assuming the presence of DC reactors to distinguish external disturbances.

A multiple behavioral model-based approach has been developed in [27]. Universal line models are derived for a finite set of possible fault cases. These models are combined in a bank of Kalman filters used to perform the fault identification. Measurements from the relay are then compared to the predictions obtained from the filters. The best predicting filter provides an estimate of the fault characteristics. This technique requires considering many filters so as to be able to identify faults with a large variety of characteristics, see [27].

Model-based algorithms are hence considered for fault localization as well as identification. Nevertheless, finding a good trade-off between quick detection and identification and accurate (therefore complex) estimation of the fault characteristics is still challenging.

3. Problem formulation and proposed approach

This section describes the problem formulation and provides an overview of the proposed approach.

3.1. Problem formulation

Consider an MTDC grid described by a graph $\mathcal{G} = (\mathcal{V}, \mathcal{E})$, where $\mathcal{E}$ is a set of edges, representing the lines connecting pairs of nodes represented by the vertices in $\mathcal{V}$. The nodes may consist of converter stations or other equipments such as sensors, relays, etc. Transmission lines can be overhead lines (OHL), underground cables, or a combination of both. Consider some vertex $q \in \mathcal{V}$ connected to n_q lines. Within the node represented by q, each line is assumed to be monitored by some fault identification device (FID) in charge of determining whether the line under protection is faulty. Each node contains thus n_q FID, each dedicated to an incoming line.

Consider a fault occurring at some time instant t_f on a given line $e = (q, q') \in \mathcal{E}$ of length $d_{qq'}$ connecting stations q and q' of the grid. The distance of the fault to stations q and q' along the line e is $d_{\mathrm{f},q}$ and $d_{\mathrm{f},q'}$, respectively with

$$d_{\mathrm{f},q} + d_{\mathrm{f},q'} = d_{qq'}. \tag{1}$$

The fault is assumed to be characterized by its pole-to-ground or pole-to-pole impedance Z_f depending on the type of fault, considered constant during the time interval of interest in the order of a millisecond. The vector of parameters describing a fault is thus $\mathbf{p} = (e, d_{\mathrm{f},q}, d_{\mathrm{f},q'}, Z_\mathrm{f}, t_\mathrm{f})^\mathrm{T}$.

Assume that the FID of station q monitoring line e acquires at a frequency f voltage and current measurements $(v_{q,e}(t), i_{q,e}(t))$ at the end of e connected to q. Using tools presented, *e.g.*, in [17], the FID is able to determine whether the grid behaves normally or not. Let $t_{\mathrm{d},q} > t_\mathrm{f}$ denotes the time instant at which an abnormal behavior is detected at station q.

Once such abnormal behavior has been detected, the FID has to determine, using all available information, whether or not the fault occurred in the line under protection.

3.2. Overview of the proposed approach

In the proposed approach (see Figure 2), an ML estimate of the vector of parameters $\mathbf{p}$ characterizing the fault is evaluated using the voltage and current measurements $(v_{q,e}(t), i_{q,e}(t))$. For that purpose, a parametric model of the voltage and current evolution at node q is considered in case of fault occurrence. This model depends on the characteristics of the grid, which are supposed known, and on the unknown vector of fault parameters $\mathbf{p}$. For a given value of $\mathbf{p}$, the output at time t of the parametric model is denoted as $\left(v^\mathrm{m}_{q,e}(\mathbf{p}, t), i^\mathrm{m}_{q,e}(\mathbf{p}, t)\right)$. As will be seen in Section 4, the considered model combines a knowledge-based model derived from physical principles and a behavioral model used to take into account additional effects such as the soil resistivity.

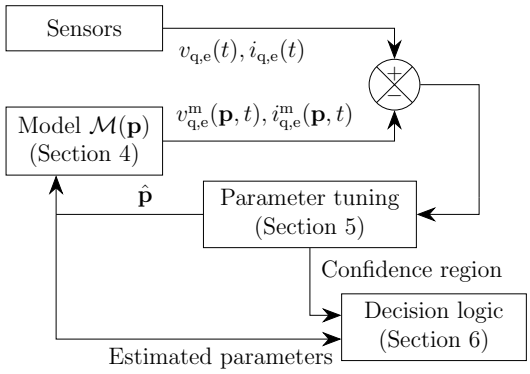

Figure 2: Overview of the proposed fault parameter vector estimation approach. Subscripts q and e are omitted to lighten the notations.

Assuming that the fault actually occurred on the line e, the FID evaluates an estimate $\widehat{\mathbf{p}}$ of the fault parameter vector $\mathbf{p}$. This estimation is performed recursively: $\widehat{\mathbf{p}}$ is updated when new measurements are available. The parameter estimation algorithm is detailed in Section 5. For each estimated parameter vector $\widehat{\mathbf{p}}$, an approximate confidence region is evaluated. An hypothesis test is then considered involving the estimate $\widehat{\mathbf{p}}$ and its confidence region to determine whether a fault actually occurred in the line e. The hypothesis test may conclude that the fault affects line e, in which case a selective clearing strategy is triggered. When it is unable to conclude, the FID waits for the availability of additional measurements to update $\widehat{\mathbf{p}}$ and the associated confidence region. Once enough measurements have been made available without allowing the FID to conclude, the fault, if it exists, is deemed to be located elsewhere in the grid. The hypothesis test and the decision logic are detailed in Section 6.

4. DC Fault analytic modeling

This section presents the model introduced to describe the evolution of the current and voltage measured at the end of a monitored line affected by a fault. The considered model combines a knowledge-based model, involving the telegraph equations, described in Section 4.1, and a behavioral model, to account for the effect of soil resistivity, described in Section 4.2. This two-stages model approach is summarized in Figure 3. The output of the knowledge-based model serves as input of the behavioral model. To simplify presentation, the case of an asymmetric monopole with single conductor overhead lines is considered. The approach can be extended to the case of underground cables or lines consisting of several types of interconnected transmission lines.

4.1. Physical modeling

This section describes the knowledge-based part of the model presented in Figure 3.

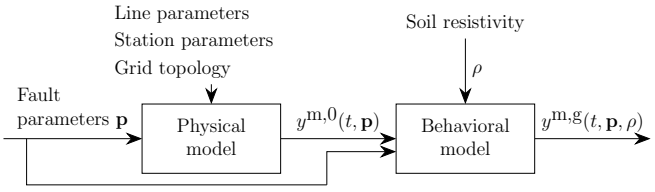

Figure 3: Combined knowledge-based (physical) and behavioral model

4.1.1. Description of traveling waves

Consider a line $e = (q, q')$ belonging to a meshed grid as presented in Figure 1. The evolution of current and voltage measured at a given point of e can be modeled using traveling waves, as shown in [28]. Along the line, current and voltage satisfy the telegraph equations, expressed in the Laplace domain as

$$\frac{\partial^2 V}{\partial x^2} = Z(s)Y(s)V(x,s) \tag{2}$$

$$\frac{\partial^2 I}{\partial x^2} = Y(s)Z(s)I(x,s), \tag{3}$$

where $Z(s) = R + sL$ and $Y(s) = G + sC$ are the transfer functions of the distributed series impedance and shunt admittance, respectively. When a fault occurs, two voltage and current waves $V_{q,1}$ and $V_{q',1}$ starting from the fault location travel along the line towards node q and q', respectively. They undergo a certain attenuation and distortion according to some propagation function H

$$V_{q,1}(s, d_q) = H(s, d_q)\, V_{\mathrm{init}}(s) \tag{4}$$

$$V_{q',1}(s, d_{q'}) = H(s, d_{q'})\, V_{\mathrm{init}}(s), \tag{5}$$

where V_{init} is the initial surge at fault location and $(d_q, d_{q'})$ are the traveled distances from the fault towards the two stations, respectively. H can be expressed, for a traveled distance d along the line, as

$$H(s, d) = \exp\left(-\sqrt{Y(s)Z(s)}d\right). \tag{6}$$

Any voltage traveling wave V has an associated current wave defined as

$$I(s, d) = Z_c^{-1}(s)V(s, d),$$

where the characteristic impedance Z_{c} is

$$Z_c(s) = \sqrt{Z(s)/Y(s)}. \tag{7}$$

When a change of propagation medium occurs (typically at the junction between a line and a station), the incident wave V_{f} gives rise to a transmitted and a reflected wave, V_{t} and V_{r} respectively. The associated voltage V_{tot} at the media change point is then

$$\begin{aligned} V_{\mathrm{tot}} &= V_{\mathrm{t}} = V_{\mathrm{f}} + V_{\mathrm{r}} \\ &= (1 + K)\, V_{\mathrm{f}} \\ &= TV_{\mathrm{f}}, \end{aligned} \tag{8}$$

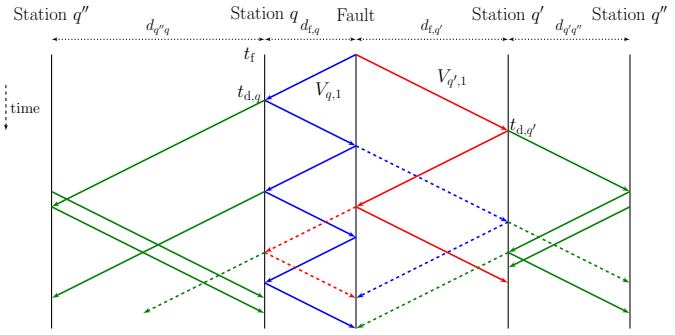

Figure 4: Example of a Bewley lattice diagram.

where the transmission and reflection coefficients T and K depend on the characteristic impedances of the media. For a wave traveling from a medium of characteristic impedance Z_1 to a medium of characteristic impedance Z_2, one has

$$K_{1\to 2} = \frac{Z_2 - Z_1}{Z_2 + Z_1} \text{ and } T_{1\to 2} = \frac{2Z_2}{Z_2 + Z_1}. \tag{9}$$

If the junction connects more than two conductors, the transmission and reflection coefficients must be adapted accordingly. Consider a wave from medium 1 of characteristic impedance Z_1 propagating to $n-1$ media of characteristic impedance $Z_2, \ldots, Z_n$. The reflection coefficient as seen from medium 1 becomes

$$K_{1\to 2\ldots n} = \frac{1/Z_1 - \sum_{\ell=2}^{n} 1/Z_\ell}{\sum_{\ell=1}^{n} 1/Z_\ell}. \tag{10}$$

Similarly, the transmission coefficient from medium 1 to ℓ is

$$T_{1\to \ell} = 1 + K_{1\to 2\ldots n} = \frac{2/Z_1}{\sum_{\ell=1}^{n} 1/Z_\ell}. \tag{11}$$

Using the reflection and transmission coefficients as well as the propagation functions as described before one can evaluate the incident, reflected, and transmitted traveling waves with the help of a Bewley lattice diagram [29]. Such diagram is presented in Figure 4 for the case of a three station network, as presented in Figure 1, connecting stations q, q', and q''. The station q'' is represented on both sides of the diagram.

4.1.2. Lossless line model and converter stations

This section describes how time-domain expression of the traveling waves are obtained for a line e connecting two power stations q and q' represented in Figure 1. For that purpose, a lossless line model is considered and the MMC are represented by RLC equivalents. The effect of soil resistivity in the ground return path is temporarily neglected, so that the distributed series impedance Z and shunt admittance Y in (6) depend only on the overhead line characteristics and do not vary significantly with the frequency, see Appendix Appendix A.

To describe the transient behavior of voltage and current once a fault has occurred, the series resistance R and shunt conductance G are neglected compared to the effects of the series inductance L and shunt capacitance C. The validity of this assumption is investigated in Appendix Appendix A. With this lossless model, (6) and (7) become

$$H(s) = \exp\left(-s\sqrt{LC}d\right) \tag{12}$$

and

$$Z_c = \sqrt{L/C}. \tag{13}$$

Modular Multilevel Converters (MMC) are considered within each station. If the current increases to 2 p.u., power electronics within the MMC will protect by auto-blocking, see [30]. When considering only the two or three first incident, reflected, and transmitted waves due to the fault, it is reasonable to consider auto-blocking as inactive at the arrival times of those waves. This is further detailed in Appendix Appendix B. With this assumption, the RLC model

$$Z_{\mathrm{mmc}}(s) = R_{\mathrm{mmc}} + sL_{\mathrm{mmc}} + \frac{1}{sC_{\mathrm{mmc}}} \tag{14}$$

for the MMC introduced in [31] can be employed. The fault may be represented by a voltage source in series with an impedance Z_{f} between ground and the fault location connected at the fault instant t_{f}. The fault impedance accounts for different effects such as the electric arc, the tower grounding impedance, and the resistance of additional unknown objects in the current path. Here, as in [32], these effects are described considering a single unknown fault resistance, *i.e.*, $Z_{\mathrm{f}} = R_{\mathrm{f}}$. Consequently, the fault leads to the initial surge at the fault location

$$V_{\mathrm{init}}(s, t_{\mathrm{f}}, Z_{\mathrm{f}}) = -v_{\mathrm{bf}} \frac{Z_{\mathrm{c}}}{Z_{\mathrm{c}} + 2R_{\mathrm{f}}} \exp(-st_{\mathrm{f}}). \tag{15}$$

The voltage source has an amplitude opposite to the voltage v_{bf} at the fault location just before its occurrence. Note that v_{bf} is not available at t_{f}. Nevertheless, assuming steady-state conditions line just before t_{f}, voltage and current along the line may be described by telegraph equations in steady state

$$\frac{\partial^2 V}{\partial x^2} = RGV. \tag{16}$$

Typically, the values of R and G are small enough, see Section 7, to neglect the variations of the voltage along lines, even of several hundreds of kilometers long. Consequently, v_{bf} can be approximated by the steady-state voltage $v\left(t_{\mathrm{d}}^{-}\right)$ measured at the relay just before the fault detection.

Hence knowing the characteristics of the different lines, stations, and the topology of the grid one can establish the expressions in the Laplace domain for any traveling waves. For example, considering a typical faulty line e connecting stations q and q' of a grid such as that represented in Figure 1, the evolution of the current and voltage at station q has to account for several traveling waves:

- due to the first incident wave from the fault to station q; this wave is reflected by station q and by the fault (plain blue lines in Figure 4),
- due to the first incident wave from the fault to station q', reflected by station q', and transmitted by the fault (dashed red lines in Figure 4),
- due to the transmission of the incident waves to other lines of the grid or which have been transmitted several times by the fault (dashed blue and green lines in Figure 4).

Consider first the traveling waves represented by the solid blue lines in Figure 4. The n^{th} forward and return waves at the station q due the reflections at the fault location can be expressed as a function of the fault parameters $\mathbf{p}$ as

$$\begin{cases} V_{\text{f},n}(s,\mathbf{p}) = (K_q K_{\text{f}})^{n-1} H\left(s, d_{\text{f},q}\right)^{2n-1} V_{\text{init}}\left(s, t_{\text{f}}\right) \\ V_{\text{r},n}(s,\mathbf{p}) = K_q V_{\text{f},n}\left(s,\mathbf{p}\right) \end{cases} \tag{17}$$

where K_q is the reflection coefficient from the line to the station q and K_{f} is the reflection coefficient at the fault, both given by (10).

Consider now the traveling waves represented by the dashed red lines in Figure 4. The first incident wave from the fault to station q' (red lines in Figure 4) is reflected by station q' and transmitted through the fault. This transmitted wave can be described at the station q as

$$\begin{cases} V'_{\text{f},n}(s,\mathbf{p}) = K_{q'} T_{\text{f}} H\left(s, 2d_{qq'} - d_{\text{f},q}\right) V_{\text{init}}\left(s, t_{\text{f}}\right) \\ V'_{\text{r},n}(s,\mathbf{p}) = K_q V'_{\text{f},n}\left(s,\mathbf{p}\right) \end{cases} \tag{18}$$

where $K_{q'}$ is the reflection coefficient from the line to the station q' and T_{f} is the transmission coefficient at the fault, given by (11).

Using the previous methodology, one can then get back to temporal domain expressions using inverse Laplace transform. Examples of time-domain expressions for the first wave (17) at station q are

$$v_{\text{f},1}(t) = -\frac{v_{\text{bf}}\, R_{\text{f}}}{Z_{\text{c}} + 2\, R_{\text{f}}}\, u\left(t - t_{\text{d},q}\right) \tag{19}$$

and

$$v_{\text{r},1}(t) = \frac{2\sqrt{C_{\text{mmc}}}\, v_{\text{bf}}\, {Z_{\text{c}}}^2}{\left(Z_c + 2\, R_{\text{f}}\right) A} \sinh\left(\frac{\left(t - t_{\text{d},q}\right) A}{4\sqrt{C_{\text{mmc}}}\, L_{\text{mmc}}}\right) \times \exp\left(-\frac{\left(2\, R_{\text{mmc}} + Z_{\text{c}}\right)\left(t - t_{\text{d},q}\right)}{4\, L_{\text{mmc}}}\right) u\left(t - t_{\text{d},q}\right) \tag{20}$$

where $A = \sqrt{C_{\text{mmc}}(2R_{\text{mmc}} + Z_{\text{c}})^2 - 16 L_{\text{mmc}}}$ is a scalar coefficient depending only on the line surge impedance and the MMC parameters. The time $t_{\text{d},q}$ is the detection time corresponding to the arrival time of the first wave at station q. It can be expressed as a function of the fault time t_{f}, the fault distance $d_{\text{f},q}$, and the wave speed $c_{\text{w}} = 1/\sqrt{LC}$;

$$t_{\text{d},q} = t_{\text{f}} + \frac{d_{\text{f},q}}{c_{\text{w}}}. \tag{21}$$

Similar expressions can be obtained for the other waves due to reflections at the fault and for waves due to reflections at other stations. The total voltage at the station is then the sum of the measured prior fault voltage $v(t = t^-_{\text{d},q})$ and the different waves arriving at the station as derived using the Bewley diagram, see Figure 4.

$$v_{\text{tot}}(t,\mathbf{p}) = v(t^-_{\text{d},q}) + v_{\text{f},1}(t,\mathbf{p}) + v_{\text{r},1}(t,\mathbf{p}) + v_{\text{f},2}(t,\mathbf{p}) + \dots \tag{22}$$

The number of reflections that must be taken into account results in a trade-off between the complexity and desired time validity interval of the model. Since the characteristic impedance is scalar, the current reaching the MMC from the monitored line is deduced from the voltage

$$i_{\text{tot}}(t,\mathbf{p}) = i(t^-_{\text{d},q}) + Z_c^{-1}(v_{\text{f},1}(t,\mathbf{p}) - v_{\text{r},1}(t,\mathbf{p}) + v_{\text{f},2}(t,\mathbf{p}) \dots). \tag{23}$$

The expressions (19), (20) and (22), (23) depend on the known characteristics of the grid, and on measured quantities such as the detection time as well as the voltage and current just before the occurrence of the fault. As mentioned in Section 3, these expressions also depend on the fault parameter vector $\mathbf{p} = (e, d_{\text{f,q'}}, d_{\text{f,q}}, R_{\text{f}}, t_{\text{f}})^{\text{T}}$ which value has to be identified.

4.2. Accounting for the soil resistivity

The knowledge-based model introduced in Section 4.1.1 neglects the effect of the soil resistivity. This section introduces a behavioral model that supplements the physical model to take into account soil resistivity effects.

Here, the soil resistivity is assumed to be represented by a known constant parameter ρ along the return path of the monitored line. While different approaches to model physically the behavior of the ground exist (see for instance [33]), to the best of our knowledge they do not lead to an analytic temporal expression of the current and voltage transient evolution. To account for soil resistivity effects, we supplement the knowledge-based model of Section 4.1.1 with a behavioral model, to get a *combined* model, see Figure 3.

Assume that $y^{\text{m},0}\left(\mathbf{p},t\right) = \left(v^{\text{m},0}\left(\mathbf{p},t\right)^T, i^{\text{m},0}\left(\mathbf{p},t\right)^T\right)^T$ is the output of the knowledge-based model in Section 4.1.1, representing the voltage and current at a given point of the monitored line e. Preliminary simulations have shown that the soil resistivity impacts the model output $y^{\text{m},0}\left(\mathbf{p},t\right)$ as a low-pass filter. Consequently, the output $y^{\text{m,g}} = \left(v^{\text{m,g}}\left(\mathbf{p},t\right)^T, i^{\text{m,g}}\left(\mathbf{p},t\right)^T\right)^T$ of the model accounting for the effects of the soil resistivity is described as

$$y^{\text{m,g}}(\mathbf{p},\rho,t_k) = G\left(z^{-1}\right) y^{\text{m},0}\left(\mathbf{p},t_k\right), \tag{24}$$

with $G(z^{-1}) = \frac{B(z^{-1})}{A(z^{-1})}$ is a transfer function, where

$$A\left(z^{-1}\right) = 1 - a_1 z^{-1} - \cdots - a_{n_a} z^{-n_a} \tag{25}$$

is an auto-regressive part that represents the inductive effect of the soil resistivity, while

$$B(z^{-1}) = z^{-n_d}\left(b_0 + b_1 z^{-1} + \cdots + b_{n_b} z^{-n_b}\right) \tag{26}$$

is a exogenous part that takes $y^{m,0}(\mathbf{p}, t_k)$ as external input. The coefficients n_a and n_b are the orders of the polynomials A and B respectively, while n_d models the input-output delay.

An offline estimation of n_d and of the coefficients a_i and b_i may then be performed considering the measurements $y(t) = \left(v(t)^T, i(t)^T\right)^T$ for a vector of known fault parameters $\mathbf{p}$ using, *e.g.*, the Electro-Magnetic Transient (EMT) software EMTP-RV [11]. Using (24), the outputs accounting for the soil resistivity provided by EMTP-RV are assumed to be described by

$$A(z^{-1})y(t_k) = B(z^{-1})y^{m,0}(\mathbf{p}, t_k) + \varepsilon(t_k), \tag{27}$$

where $\varepsilon(t)$ represents the measurement error term and all effects not captured by the model (24). Then, for given values of the fault parameter vector $\mathbf{p}$ and of ρ, a least-squares estimate of n_d and of the parameters a_i, b_i has been performed [34].

The coefficients of the transfer function G which models the effect of soil resistivity clearly depend on the value of ρ. Moreover, additional simulations have also evidenced the impact of the components of the fault parameter vector $\mathbf{p}$, among which the distance to the fault d_f is the most important. In order to get a behavioral model of the impact of the soil resistivity that is valid whatever the fault location, one explicitly accounts for d_f in the parameters a_i and b_i of the model.

Low order models have proven to give a relatively good fit of the simulated voltage and currents from EMTP. In the case of a first order low pass filter, the coefficients a_1, b_0 and n_d can be estimated for different values of the fault distance d_f and a given value of ρ, considering only the first traveling wave generated by a fault.

the following model

$$a_1^m(d_f) = \alpha_{1,0} + \alpha_{1,1} d_f^{-1} + \alpha_{1,2} d_f^{-2} \tag{28}$$

$$b_0^m(d_f) = \beta_{0,0} + \beta_{0,1} d_f^{-1} + \beta_{0,2} d_f^{-2} \tag{29}$$

$$n_d^m(d_f) = \text{Round}\left(\nu_0 + \nu_1 d_f^1 + \nu_2 d_f^2\right) \tag{30}$$

of the evolution of a_1, b_0 and n_d with d_f depending on the parameters vectors $\boldsymbol{\alpha}_1 = (\alpha_{1,0}, \alpha_{1,1}, \alpha_{1,2})^T$, $\boldsymbol{\beta}_0 = (\beta_{0,0}, \beta_{0,1}, \beta_{0,2})^T$ and $\boldsymbol{\nu} = (\nu_0, \nu_1, \nu_2)^T$ has been adjusted by least-squares estimation.

A comparison of the output of the complete model with that of the knowledge-based model is provided in Section 7. The estimation of the filter coefficients $a_1^m(d_f)$, $b_0^m(d_f)$, and $n_d^m(d_f)$ is also described.

4.2.1. Other traveling waves

To account for the effect of soil resistivity on other traveling waves, the distance d in the parameters $a_1^m(d)$ and $b_0^m(d)$ of the model (24) has to represent the sum of the traveled distance.

For instance, the first traveling wave, once it has been reflected by the station and at the fault location, when it reaches again the station, has traveled three times the fault distance. The combined model output $y^{m,g}$ is obtained by filtering the knowledge-based model output $y^{m,0}$ with a filter G which parameters are $a_1^m(3d_f)$ and $b_0^m(3d_f)$. An example of this approach is provided in Section 7.2.3.

A possible way to model situations where a line spreads over areas with different soil resistivities, is to consider a cascade of several filters G, each tuned for subarea assumed of constant soil resistivity.

5. Estimation of the fault parameters

In this section, the estimation of the fault parameters is detailed. This step corresponds to the *parameter tuning* block of Figure 2 introduced in Section 3 and uses the parametric model described in Section 4.

Consider that an unusual behavior is detected by a relay q monitoring a line e at the time $t_{d,q}$. Assume that n voltage and current measurements $\mathbf{y}(t) = (v(t), i(t))^T$ have been performed at time t_k, $k = 1, \ldots, n$, with $t_1 \leqslant t_{d,q} < t_n$. For a given value of $\mathbf{p}$, one may evaluate the combined model outputs $\mathbf{y}^m(\mathbf{p}, t) = (v^m(\mathbf{p}, t)\ i^m(\mathbf{p}, t))^T$ and evaluate the output error

$$\mathbf{e}_y(\mathbf{p}, t_k) = \mathbf{y}(t_k) - \mathbf{y}^m(\mathbf{p}, t_k),\ k = 1, \ldots, n. \tag{31}$$

Assume that, for the true value of the fault parameters $\mathbf{p}^*$, the observed data satisfy

$$\mathbf{y}(t_k) = \mathbf{y}^m(\mathbf{p}^*, t_k) + \varepsilon(t_k),\ k = 1, \ldots, n \tag{32}$$

where ε_k belongs to a sequence of realizations of independent random vectors that follows a zero-mean Gaussian distribution with known covariance matrix

$$\Sigma = \begin{pmatrix} \sigma_v^2 & 0 \\ 0 & \sigma_i^2 \end{pmatrix}, \tag{33}$$

where σ_v^2 and σ_i^2 are obtained from the characteristics of the voltage and current sensors. The ML estimate of $\mathbf{p}$ from n observations is

$$\widehat{\mathbf{p}} = \arg\max_{\mathbf{p}} \pi\left(\mathbf{y}(t_1), \ldots, \mathbf{y}(t_n) | \mathbf{p}\right), \tag{34}$$

see [35]. With the considered measurement noise model, evaluating $\widehat{\mathbf{p}}$ requires the minimization of the cost function

$$c^{(n)}(\mathbf{p}) = \mathbf{f}^{(n)}(\mathbf{p})^T \left(\widetilde{\Sigma}^{(n)}\right)^{-1} \mathbf{f}^{(n)}(\mathbf{p}), \tag{35}$$

where

$$\mathbf{f}^{(n)}(\mathbf{p}) = \Big[(v(t_1) - v^{\mathrm{m}}(\mathbf{p}, t_1)), \ldots, (v(t_n) - v^{\mathrm{m}}(\mathbf{p}, t_n)) \\ (i(t_1) - i^{\mathrm{m}}(\mathbf{p}, t_1)), \ldots, (i(t_n) - i^{\mathrm{m}}(\mathbf{p}, t_n))\Big]^T, \quad (36)$$

and

$$\widetilde{\Sigma}^{(n)} = \mathrm{diag}\left(\sigma_{\mathrm{v}}^2, \ldots, \sigma_{\mathrm{v}}^2, \sigma_{\mathrm{i}}^2, \ldots, \sigma_{\mathrm{i}}^2\right). \quad (37)$$

In the parameter estimation process, the first component e of $\mathbf{p}$ is assumed fixed when trying to decide whether the fault has occurred in the monitored line e or not. Moreover, $d_{\mathrm{f},q'}$ can be deduced from (1). Finally the fault occurrence time t_{f} and the fault distance $d_{\mathrm{f},q}$ are related to the detection time $t_{\mathrm{d},q}$ using (21). Since $t_{\mathrm{d},q}$ can be measured, only two parameters $d_{\mathrm{f},q}$ and R_{f} are left to be determined.

For a given number of observations n, iterative optimization techniques (Gauss-Newton, Levenberg-Marquardt) may be used to build a sequence of parameter estimates

$$\mathbf{p}_{k+1}^{(n)} = \mathbf{p}_k^{(n)} + \boldsymbol{\delta}_k^{(n)}, \quad (38)$$

where $\boldsymbol{\delta}_k^{(n)}$ is some correction term such that $c^{(n)}(\mathbf{p}_{k+1}^{(n)}) < c^{(n)}(\mathbf{p}_k^{(n)})$, starting from an initial estimate $\mathbf{p}_0^{(n)}$. For example, with the Gauss-Newton method, one has

$$\boldsymbol{\delta}_k^{(n)} = -\left(J_f^{(n)T}\left(\widetilde{\Sigma}^{(n)}\right)^{-1} J_f^{(n)}\right)^{-1} J^{(n)T}\left(\widetilde{\Sigma}^{(n)}\right)^{-1} \mathbf{f}^{(n)}, \quad (39)$$

where $J_f^{(n)}$ is the Jacobian matrix of $\mathbf{f}^{(n)}$ with respect to $\mathbf{p}$ evaluated at $\mathbf{p}_k^{(n)}$. The computation of the Jacobian matrix can be done explicitly for the physical model as well as the combined model, due to their (relative) simplicity.

Assume that after κ iterations (38), n' measurements are available, with $n' = n + \Delta n$. The cost function $c^{(n)}(\mathbf{p})$ is updated to $c^{(n')}(\mathbf{p})$. Then κ new iterates (38) are performed starting from $\mathbf{p}_0^{(n')} = \mathbf{p}_\kappa^{(n)}$. In practice, κ and the number of additional measurements Δn required to update the cost function may be tuned to reach a compromise between speed and accuracy of the estimation process.

The estimation algorithm is run until a stopping condition is satisfied, as detailed in Section 6.

6. Fault identification: decision logic

This section presents the logic that allows the algorithm to decide whether a fault actually occurred on the protected line or not. This step corresponds to the *decision logic* block of Figure 2 introduced in Section 3.

After each iteration, the algorithm determines whether it has obtained a satisfying estimate of the fault parameters with a good level of confidence, indicating that the monitored line is faulty. The algorithm may also stop once it has performed a maximum number of iterations, corresponding to a maximum measurement window. In the latter case, the fault is considered to be outside the protected line, or to be non-existent. To determine whether the estimate is consistent with the hypothesis that the monitored line is faulty, two tests are considered. First, a *validity* test determines whether or not the value of the estimated parameter vector is included in some domain of interest. Second, an *accuracy* test determines if the confidence region associated to the estimate is small enough. In this section the number n of observed data is omitted to lighten the notations.

First, the estimated parameters must belong to a certain domain of interest $\mathcal{D}_{\mathbf{p}}$ which represents plausible values for the fault parameters. $\mathcal{D}_{\mathbf{p}}$ may be defined as

$$\mathcal{D}_{\mathbf{p}} = \{(d_{\mathrm{f}}, R_{\mathrm{f}}) | d_{\mathrm{f,min}} \leq d_{\mathrm{f}} \leq d_{\mathrm{f,max}}, R_{\mathrm{f,min}} \leq R_{\mathrm{f}} < R_{\mathrm{f,max}}\} \quad (40)$$

where $(d_{\mathrm{min}}, d_{\mathrm{max}})$ defines the portion of the line actually monitored by the relay and $(R_{\mathrm{f,min}}, R_{\mathrm{f,max}})$ the range of fault resistance that requires fast decision, since a high value of R_{f} corresponds to a non-critical fault for which more time is available to take action, as investigated in [19]. Typical boundary values are $d_{\mathrm{f,min}} = 0\,\mathrm{km}$, $d_{\mathrm{f,max}} = 90\,\% d_{qq'}$ and $R_{\mathrm{f,min}} = 0\,\Omega$, $R_{\mathrm{f,max}} = 200\,\Omega$.

Second, in the accuracy test, for each estimate $\mathbf{p}_k$ of $\mathbf{p}^*$ belonging to $\mathcal{D}_{\mathbf{p}}$, an associated confidence region is evaluated. Various approaches for this evaluation are available, see, *e.g.*, [36, 35]. Here, one approximates the covariance matrix

$$P_{\mathrm{ML}} = E_{\mathbf{y}|\mathbf{p}^*}\left\{(\mathbf{p}_k - \mathbf{p}^*)(\mathbf{p}_k - \mathbf{p}^*)^T\right\} \quad (41)$$

of the estimate $\mathbf{p}_k$ by its Cramér-Rao Lower Bound (CRLB)

$$P_{\mathrm{ML}} \simeq I^{-1}(\mathbf{p}^*), \quad (42)$$

where

$$I(\mathbf{p}) = -E_{\mathbf{y}|\mathbf{p}}\left\{\frac{\partial^2 \ln \pi_y(\mathbf{y}|\mathbf{p}))}{\partial \mathbf{p} \partial \mathbf{p}^T}\right\} \quad (43)$$

is the Fisher information matrix. This approximation relies on assumptions that are in general not satisfied in practice. Usually, the measurement noise is considered as independent and identically distributed with zero-mean Gaussian distribution. Moreover, the model error has to be small compared to the measurement noise. Finally, $I^{-1}(\mathbf{p}^*)$ is replaced by $I^{-1}(\mathbf{p}_k)$ in (42), since $\mathbf{p}^*$ is not available. Nevertheless, the CRLB gives a reasonable evaluation of the estimation uncertainty.

From (43), and considering the hypotheses on the measurement noise, the Fisher information matrix becomes

$$I(\mathbf{p}) = J_f^T(\mathbf{p})\,\widetilde{\Sigma}^{-1} J_f(\mathbf{p}). \quad (44)$$

When $\widetilde{\Sigma}$ is not known, its diagonal components may be obtained as the estimated variances for the current and voltage residuals

$$\widehat{\sigma}_v^2 = \frac{1}{n - n_{\mathrm{p}}} \sum_{\ell=1}^{n} \left(v(t_\ell) - v^{\mathrm{m}}(t_\ell, \mathbf{p}_k)\right)^2$$

$$\widehat{\sigma}_i^2 = \frac{1}{n - n_{\mathrm{p}}} \sum_{\ell=1}^{n} \left(i(t_\ell) - i^{\mathrm{m}}(t_\ell, \mathbf{p}_k)\right)^2,$$

with n_p the number of estimated parameters.

Specific confidence regions can be computed using the fact that $\frac{1}{n_\mathrm{p}}(\mathbf{p}-\mathbf{p}_k)^T I^{-1}(\mathbf{p}_k)(\mathbf{p}-\mathbf{p}_k)$ follows approximately a Fisher-Snedecor distribution $F(n_\mathrm{p}, 2n-n_\mathrm{p})$. Assuming that the number of observations n is large compared to the number of estimated parameters n_p, the $(1-\alpha)\%$ confidence region can be approximated by the ellipsoid

$$\mathcal{R}^\alpha(\mathbf{p}) = \left\{\mathbf{p}\in\mathbb{R}^{n_\mathrm{p}} \,|\, (\mathbf{p}-\mathbf{p}_k)^T I^{-1}(\mathbf{p}_k)(\mathbf{p}-\mathbf{p}_k) \leq \chi^2_{n_\mathrm{p}}(1-\alpha)\right\},$$

where $\chi^2_{n_\mathrm{p}}(1-\alpha)$ is the value that a random variable distributed according to a chi-square distribution with n_p degrees of freedom has a probability $1-\alpha$ to be larger than.

The volume of the $(1-\alpha)\%$ confidence ellipsoids $\mathcal{R}^\alpha(\mathbf{p})$ is then used to determine the accuracy of the current estimate $\mathbf{p}_k$ of $\mathbf{p}^*$. The estimation algorithm is deemed to have obtained an accurate estimate of the fault parameters if the volume of $\mathcal{R}^\alpha(\mathbf{p})$ is below a certain threshold

$$\mathrm{vol}\left(\mathcal{R}^\alpha(\mathbf{p})\right) \leqslant \mathrm{tr}_{1-\alpha} \tag{45}$$

The threshold $\mathrm{tr}_{1-\alpha}$ has to be tuned so as to ensure both dependability and security. The estimation algorithm has to correctly identify all faults occurring on the protected line while rejecting faults occurring elsewhere. Tuning is done heuristically considering a large number of simulated fault cases, especially limit cases where forward faults occur on an adjacent line, since they are harder to distinguish from fault occurring at the remote end of the protected line.

When both validity and accuracy tests are satisfied, the estimation algorithm stops and the fault is considered to be in the protected zone. The proposed fault identification approach using parameter estimation and the validity and accuracy tests is summarized in Algorithm 1. The algorithm starts the fault parameter estimation as soon as an unusual behavior is detected (line 3). For a given set of data, κ iterations of the estimation algorithm are run (lines 7-8). The algorithm stops and concludes that the fault is internal as soon as the estimate satisfies the stopping conditions (line 9-10). If these conditions are not met, Δn new measurement data are added when available (line 13) and the estimation process starts over from the last parameter estimate (line 14). If the maximum length of the measurement window has been reached and the stopping condition have not been satisfied, the fault is considered external (line 17). The corresponding flowchart of the algorithm is provided in Figure 5.

Algorithm 1 Fault parameter identification algorithm

1: Input: n_0, $\mathbf{p}_0$, n_max, κ
2: Output: fault in protected zone, fault parameters
3: **if** Unusual behavior detected **then**
4: Collect $n = n_0$ current and voltage measurements
5: Initialize $\mathbf{p}_0^{(n)} = \mathbf{p}_0$
6: **while** $n < n_\mathrm{max}$ **do**
7: **for** $k = 1 : \kappa$ **do**
8: Update $\mathbf{p}_{k+1}^{(n)} = \mathbf{p}_k^{(n)} + \delta_k$
9: **if** $stop\_cond(\mathbf{p}_{k+1}^{(n)}, \mathcal{R}^{(\alpha)}(\mathbf{p}_{k+1}^{(n)}))$ =true **then**
10: Fault is internal **return** (true, $\mathbf{p}_{k+1}^{(n)}$)
11: **end if**
12: **end for**
13: Wait until $n + \Delta n$ measurements are available
14: $\mathbf{p}_0^{(n+\Delta n)} = \mathbf{p}_\kappa^{(n)}$
15: $n \leftarrow n + \Delta n$
16: **end while**
17: Fault is external **return** (false, $\emptyset$)
18: **end if**

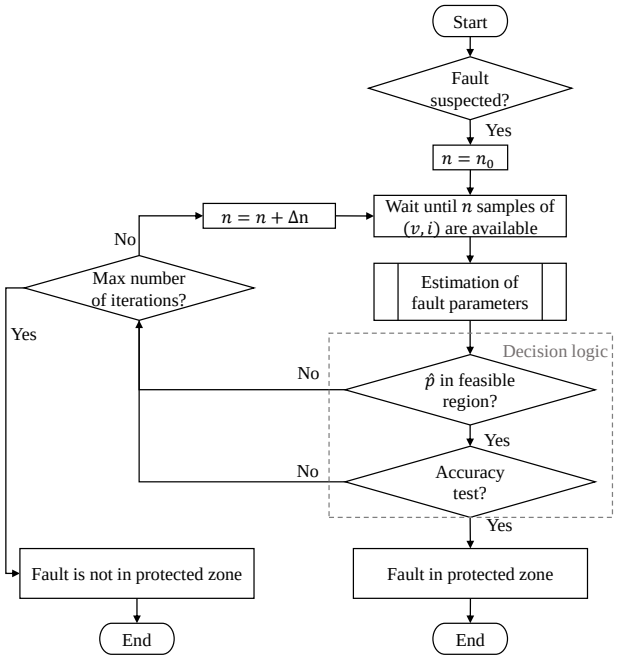

Figure 5: Flowchart of the proposed fault identification algorithm

7. Simulation results

This section presents the results obtained in simulations. Measurements in case of faults have been provided by EMTP-RV and the FID was implemented in Matlab.

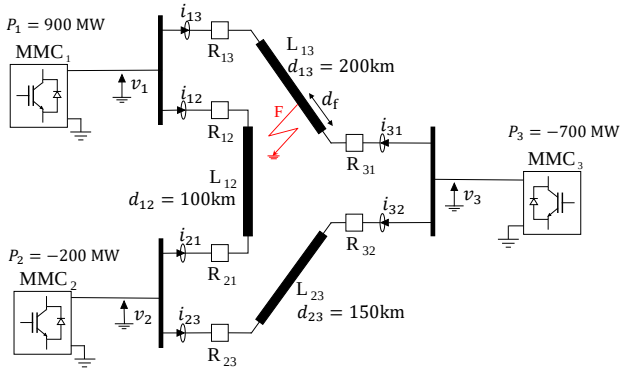

Figure 6: Test grid considered

Section 7.1 describes the considered grid and the parameters used for its model. First simulation results illustrating the model proposed in Section 4.2 are presented in Section 7.2. The behavior of the fault identification algorithm is then detailed on two fault cases in Section 7.3. Finally, extensive simulations considering a wide range of fault cases are presented in Section 7.4 to illustrate the performance of the FID algorithm.

7.1. Model of the grid

To test the proposed approach, consider the three-node Delta grid of Figure 6 with single-conductor identical overheadlines and 3 MMC stations. Such type of grid may constitute an elementary part of more complex meshed grids described, *e.g.*, in [4]. As will be seen in the experimental part, the proposed algorithm can characterize the fault parameters in much less than 1 ms after the fault occurrence. If the three-node Delta grid would actually be part of a more complex grid, the impact of the presence of further links would be negligible in the first few hundreds of micro seconds after the fault occurrence. Consequently, results obtained with the considered grid are likely to be representative of results obtained with a more complex grid.

Relays R_{13} and R_{31} monitor line L_{13} of length $d_{13} = 200\,\text{km}$; Relays R_{23} and R_{32} monitor line L_{23} of length $d_{23} = 150\,\text{km}$; Relays R_{12} and R_{21} monitor line L_{12} of length $d_{13} = 100\,\text{km}$. Numerical values for the station and line characteristics are given in Tables 1 and 2. The active power injected by each converter stations prior to the fault is indicated for each station in Figure 6. The MMCs are simulated with switching function of arms [37] and a wide-band model is used for the transmission lines [38]. The current and voltage sensors used in the EMT simulations have an accuracy class of 1 %, a bandwidth of 300 kHz, a sampling frequency of 1 MHz, and a resolution of 16 bits. Further details on sensor and relay configurations can be found in [4].

From Tables 1 and 2, one can evaluate the parameters used in the knowledge-based model presented in Section 4 such as the distributed parameters of the line, see Table 4, and the RLC model of the stations, see Table 3.

Table 1: Characteristics of the MMC stations

Rated power (MW)	1000
DC rated voltage (kV)	320
Arm inductance (p.u.)	0.15
Transformer resistance (p.u.)	0.001
Capacitor energy in each submodule (kJ/MVA)	40
Conduction losses of each IGBT/diode (Ω)	0.001
Number of sub-modules per arm	400

Table 2: Overhead-line characteristics

	L_{13}	L_{12}	L_{23}
DC resistance (mΩ/km)		24	
Outside diameter (cm)		4.775	
Horizontal distance (m)		5	
Vertical height at tower (m)		30	
Vertical height at mid-span (m)		10	
Soil resistivity (Ωm)		100	

7.2. Evaluation of the model accuracy

This section evaluates the accuracy of the complete model of Section 4, including the behavioral part of the model representing the impact of the soil resistivity.

7.2.1. First traveling wave

Figure 7 represents an example of the evolutions of voltage and current for the first traveling wave generated by a fault occurring on line L_{13} at time $t_f = 0$, with a resistance of 20 Ω situated 50 km away from the station 3. The soil resistivity is taken as $\rho = 100\,\Omega\text{m}$, which is a low or average value according to [39].

The estimation of the model parameters has been performed considering only the first traveling wave generated by a fault. It can be observed that the outputs of the combined model accounting for the soil resistivity ($\rho > 0$) are much closer to the outputs provided by EMTP-RV than the outputs of the physical model neglecting the soil resistivity ($\rho = 0$). For the considered behavioral model $G\left(z^{-1}\right)$, $n_d = 4$ and considering $n_a = 1$, $n_b = 0$ provides the best compromise between accuracy and complexity.

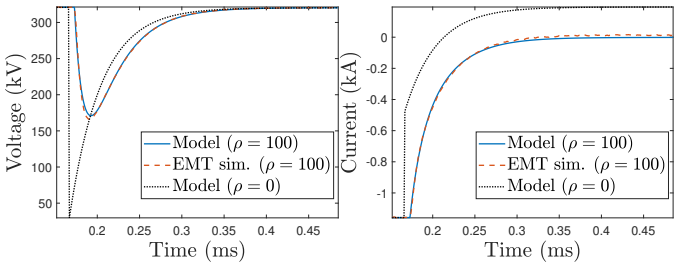

Figure 7: Comparison of the voltage (left) and current (right) transient models, neglecting or accounting for the soil resistivity with the output of an EMT simulation software; the simulated fault occurred at $t_f = 0$ and 50 km from the station with a resistance of 20 Ω; the soil resistivity is $\rho = 100\,\Omega\text{m}$.

Table 3: Equivalent parameters of the MMC stations

Equivalent inductance (mH)	8.1
Equivalent resistance (Ω)	0.4
Equivalent capacitance (μF)	391

Table 4: Overhead-line distributed parameters

	L_{13}	L_{12}	L_{23}
Series resistance R (mΩ/km)		24	
Series inductance L (mH/km)		1.45	
Shunt capacitance C (nF/km)		7.68	
Shunt conductance G (nS/km)		0.2	

7.2.2. Validity of the filter parameter fitting approach

Figure 8 describes the evolution of the coefficients a_1, b_0 and n_d of the behavioral model as estimated for different values of the fault distance d_f considering again $\rho = 100\,\Omega$m. Here again, the estimation has been performed considering only the first traveling wave generated by a fault occurring at time $t_\mathrm{f} = 0$. The evolution of $a_1^\mathrm{m}(d_\mathrm{f})$, $b_0^\mathrm{m}(d_\mathrm{f})$, and $n_\mathrm{d}^\mathrm{m}(d_\mathrm{f})$ with d_f is also provided in Figure 8, showing an excellent match with the estimated values of a_1, b_0, and n_d. It can be observed that the inductive effect, represented by the parameter a_1, increases with the fault distance. For small values of d_f, as expected, a_1 is close to 0 and the model of Section 4.1.1 neglecting the soil resistivity has good modeling performances.

7.2.3. Other traveling waves

To account for the effect of soil resistivity on other traveling waves, as indicated in Section 4.2.1, the distance d in the parameters $a_1^\mathrm{m}(d)$ and $b_0^\mathrm{m}(d)$ of the model (24) is assumed to represent the sum of the traveled distance.

Figure 9 shows the evolution of voltage and current at a station considering a fault occurring at time $t_\mathrm{f} = 0$, with a resistance of $20\,\Omega$, and situated 30 km away from the station. One observes that the match with the EMT simulation is very good for the first traveling wave and still good for this wave after two additional reflections (at the station and at the fault).

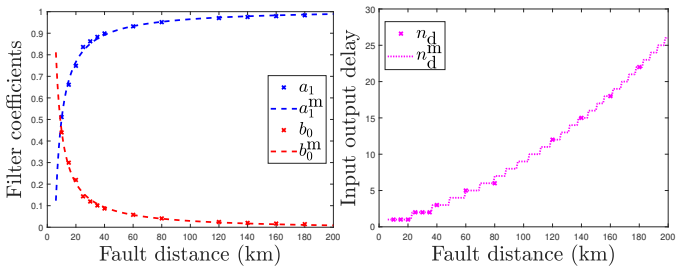

Figure 8: Evolution of the estimated parameters a_1, b_0 (left) and n_d (right) of the behavioral model G as a function of d_f (crosses), compared to their modeled evolution using $a_1^\mathrm{m}(d_\mathrm{f})$ and $b_0^\mathrm{m}(d_\mathrm{f})$ (left) and n_d^m (right) (dashed and dotted lines)

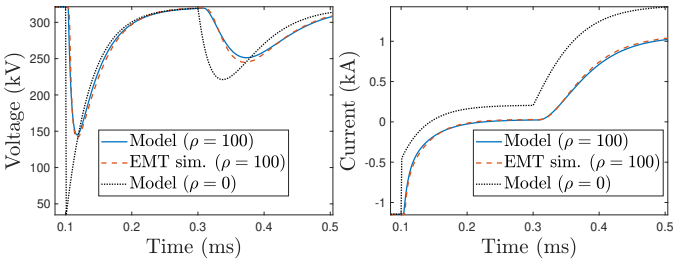

Figure 9: Comparison of the voltage (left) and current (right) transient models, neglecting or accounting for the soil resistivity with the output of an EMT simulation software; the simulated fault is located at 30 km from the station and has a resistance of $20\,\Omega$; the soil resistivity is $\rho = 100\,\Omega$m.

Table 5: Algorithm tuning parameters.

Parameter	Value
Initial point, $\mathbf{p_0}$	$R_\mathrm{init} = 1\Omega, d_\mathrm{init} = 6$km
Number of iterations for n data	$k(n) = 1$
Additional data points Δn	10
Confidence level	$1 - \alpha = 0.95$
Accuracy test threshold	$\mathrm{tr}_{0.95} = 10$
Targeted fault distances	$d_\mathrm{f,min} = 0, d_\mathrm{f,max} = 0.9d$
Targeted fault resistances	$R_\mathrm{f,min} = 0, R_\mathrm{f,max} = 200\Omega$
Maximum measurement window	$3d/c_\mathrm{w}$

7.3. First illustration of the fault identification algorithm

To illustrate the behavior of the identification algorithm, one considers two cases of pole-to-ground faults occurring between stations 3 and 1, *i.e.*, in line L_{13} of the grid in Figure. 6. Parameters of the algorithm, introduced in Sections 5, 6 and 6, are given in Table 5. Though such parameters can be adjusted, they are kept constant for all the simulations. The different parameters have been tuned considering extensive simulations, focusing on critical cases with remote faults occurring on the protected line and low impedance faults occurring on an external line close to a remote station. The maximum duration of the measurement window, which is used as stopping criterion for the estimation algorithm, varies for each relay, since it depends on the total length d of the monitored line and on the traveling wave propagation speed c_w in the line (as defined in 4). Each time $\Delta n = 10$ additional measurements are available, a single iteration of the estimation algorithm is performed, thus for all n, $\kappa(n) = 1$.

In Case 1, the fault, located at $d_\mathrm{f}^* = 30$ km from station 3 (close fault) with an impedance of $R_\mathrm{f}^* = 20\,\Omega$, occurs at $t_\mathrm{f} = 0$. Once an abnormal behavior is detected at relay R_{31} (using the approach described in [17]), the identification algorithm is started. Its behavior can be analyzed by plotting the contour of the cost function (35) to minimize at each iteration as well as the trajectory of the estimate $(d_\mathrm{f}, R_\mathrm{f})$ of the fault parameter vector, see Figure 10. The 95% confidence ellipse of the estimated parameter vector is also displayed at each step. After each iteration, new data points are added to the cost function.

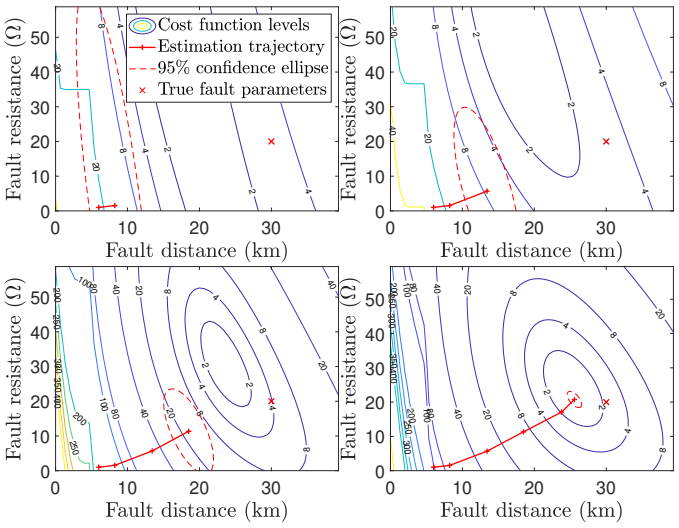

Figure 10: Case 1: fault at $d_{\mathrm{f}}^{*} = 30\,\mathrm{km}$ from station 3 (close fault) with an impedance of $R_{\mathrm{f}}^{*} = 20\,\Omega$: evolution of the contour plot of the cost function and estimated parameters at iterations 1,2,3 and 5.

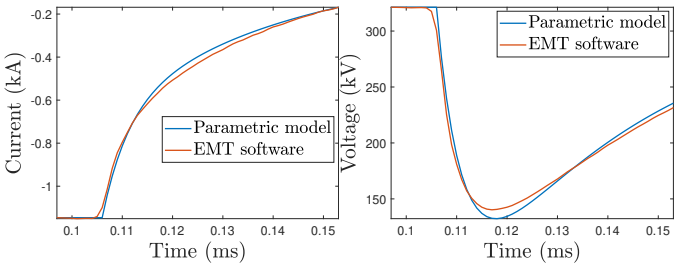

Figure 11: Case 1: Simulated current and voltage measurements compared to the combined model outputs for $\widehat{d}_{\mathrm{f}} = 26\,\mathrm{km}$ and $\widehat{R}_{\mathrm{f}} = 21\,\Omega$.

It can be observed that its minimum gets closer to $(d_{\mathrm{f}}^{*}, R_{\mathrm{f}}^{*})$ and that the cost contours concentrate around $(d_{\mathrm{f}}^{*}, R_{\mathrm{f}}^{*})$. The estimate $(d_{\mathrm{f}}, R_{\mathrm{f}})$ also gets closer $(d_{\mathrm{f}}^{*}, R_{\mathrm{f}}^{*})$ and the size of the confidence ellipsoid reduces. The estimation algorithm stops and correctly identifies the fault on the line after 5 iterations, requiring only measurements obtained in a time window of $56\,\mu\mathrm{s}$ which contains the fault detection time t_{d}. The estimated parameters are $\widehat{d}_{\mathrm{f}} = 26\,\mathrm{km}$ and $\widehat{R}_{\mathrm{f}} = 21\,\Omega$ when the algorithm stops. Nevertheless, the stopping conditions are satisfied before the minimum of the cost function is reached. This allows ultra-fast identification of the fault, which is the main objective of the protection algorithm, even though it limits the accuracy of the estimated parameters. Considering a longer measurement window of $266\,\mu\mathrm{s}$ results in the estimated parameters $\widehat{d}_{\mathrm{f}} = 30\,\mathrm{km}$ and $\widehat{R}_{\mathrm{f}} = 18\,\Omega$.

The voltage and current measurements simulated by the EMT software and at the output of the combined model for $\widehat{d}_{\mathrm{f}} = 26\,\mathrm{km}$ and $\widehat{R}_{\mathrm{f}} = 21\,\Omega$ are represented in Figure 11. One sees that the observation of the first wave is enough for an accurate fault identification.

To analyze the behavior of the identification algorithm

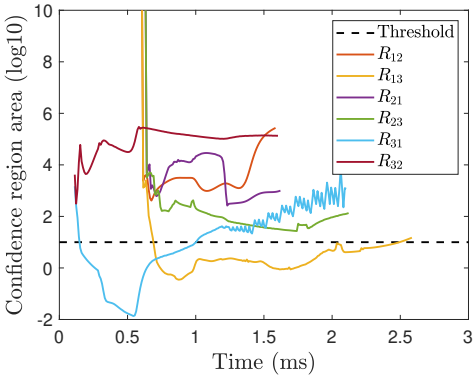

Figure 12: Case 1: Evolution of the accuracy criterion at the 6 relays.

at other relays, the evolution of the accuracy criterion at the 6 relays is plotted in Figure 12. The fault is rapidly identified at relays R_{31} and R_{13}. The evolution of the $\mathrm{vol}\,(\mathcal{R}^{\alpha}(\mathbf{p}))$ used in the accuracy criterion (45) evaluated at R_{31} and R_{13} is plotted until the maximum measurement window is reached. This facilitates comparison with the evolution of $\mathrm{vol}\,(\mathcal{R}^{\alpha}(\mathbf{p}))$ involved in the accuracy criteria evaluated at the other relays. Since the fault is close to station 3, it is first detected at relays R_{31} (monitoring line L_{13}) and R_{32} (monitoring line L_{23}). The accuracy test is satisfied at relay R_{31} after 5 iterations and the fault is identified in line L_{13}, as shown previously. It can be seen that after reaching a minimum after 0.5 ms, the confidence region area starts increasing and reaches higher values after 1 ms. This is due to the reduced number of waves included in the model which limits its time validity, as mentioned in Section 4.1. At relay R_{32} the area of the confidence region never goes below the threshold, indicating that the fault is not in line L23. At $t = 0.6\,\mathrm{ms}$ the fault is detected at the other relays. At relay R_{13}, the fault is again correctly identified after few iterations. The fault identification algorithms run at relays R_{12}, R_{21}, and R_{23} and stop when their maximum measurement window is reached. As the latter depends on the total length of the monitored line, the algorithm at relay R_{31}, monitoring line L_{13} of length $d_{13} = 200\,\mathrm{km}$ runs twice as long as the algorithm at relay R_{21}, monitoring line L_{12} of length $d_{12} = 100\,\mathrm{km}$. This illustrates that the method is able to identify internal faults using very few measurements while rejecting faults occurring on neighboring lines. Furthermore, the method is inherently directional because the direction of the current is embedded in the parametric model, see Figure 11. Faults occurring behind the relay are not confused with faults occurring on the protected line. This also justifies the insensitivity of the algorithm to bus-bar faults.

In case 2, a fault occurs at $t_{\mathrm{f}} = 0$, at a distance $d_{\mathrm{f}}^{*} = 140\,\mathrm{km}$ from station 3 (remote fault) on line L_{13} with an impedance of $R_{\mathrm{f},2}^{*} = 40\,\Omega$. In that case, the estimation algorithm at relay R_{31} requires observations of current and voltage during a time interval of $126\,\mu s$ after the detec-

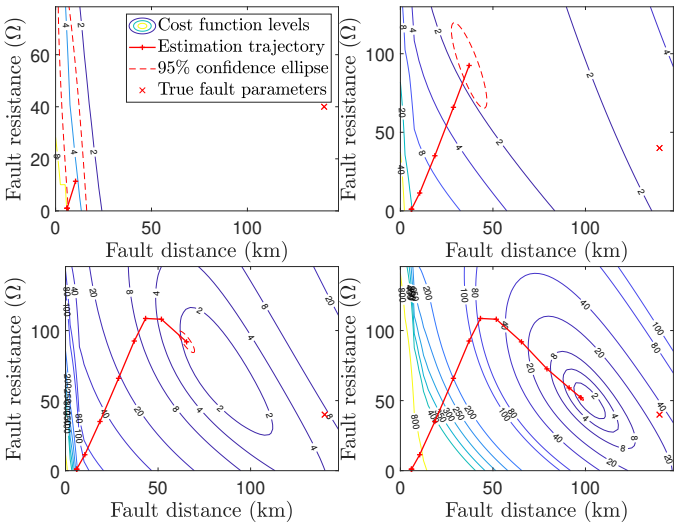

Figure 13: Case 2: fault at $d_{\mathrm{f}}^{*} = 140\,\mathrm{km}$ from station 3 (remote fault) with an impedance of $R_{\mathrm{f}}^{*} = 40\,\Omega$: evolution of the contour plot of the cost function and estimated parameters at iterations 4, 7, 9, and 11.

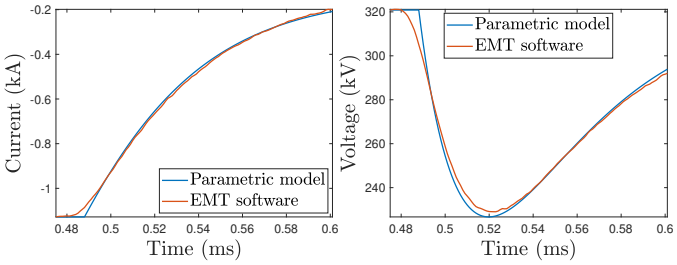

Figure 14: Case 2: Simulated current and voltage measurements compared to the combined model outputs for $\widehat{d}_{\mathrm{f}} = 97\,\mathrm{km}$ and $\widehat{R}_{\mathrm{f}} = 60\,\Omega$, when a single wave is observed.

tion of the fault. The evolution of the contour plot of the cost function to be minimized at each iteration as well as the trajectory and the 95% confidence ellipse of the estimate of the fault parameters are displayed in Figure 13. The evolution with time during the measurement window of the EMT-simulated measured voltage and current as well as those obtained using the combined model with the estimated parameters are displayed in Figure 14. Compared to case 1, the estimated parameters $\widehat{d}_{\mathrm{f}} = 98\,\mathrm{km}$ and $\widehat{R}_{\mathrm{f}} = 52\,\Omega$ are farther from the true parameters. This is partly due to the reduced precision of soil resistivity modeling when the fault distance is larger. As for case 1, a longer measurement window reduces the estimation error. For instance, a measurement window of $416\,\mu\mathrm{s}$ leads to estimated parameters $\widehat{d}_{\mathrm{f}} = 120\,\mathrm{km}$ and $\widehat{R}_{\mathrm{f}} = 32\,\Omega$.

The accuracy of the estimated fault parameters can be improved by considering longer observation windows. This is further evidenced for the fault cases 1 and 2 in Figure 15. The estimated fault distances and resistances are plotted as functions of the length of the observation window along with the actual fault parameters. The evolution of the area of the confidence region is also provided to emphasize

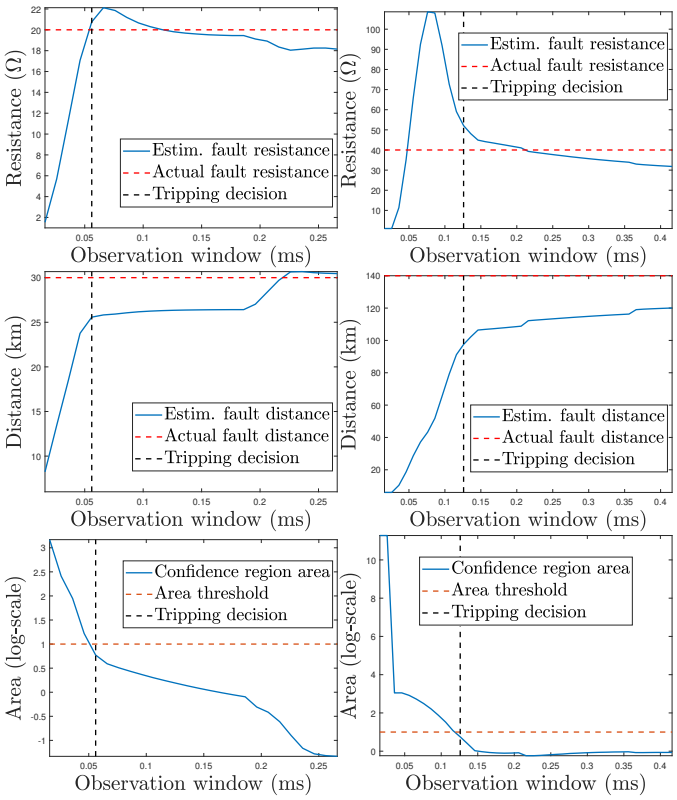

Figure 15: Evolution of the estimated parameters with the length of the observation window for fault case 1 (left) and 2 (right)

the measurement window required to identify the fault and take the tripping decision. The accuracy of the estimated parameters improves with the length of the observation windows while still considering relatively few measurement data. In particular, the arrival of an additional traveling wave brings decisive information on the fault distance, as can be seen around $t = 0.2\,\mathrm{ms}$ for the fault case 1.

7.4. Extensive simulations

More extensive simulations are now performed to analyze the behavior of the algorithm over a wider range of fault characteristics. We simulated different single fault scenarios with parameters $(R_{\mathrm{f}}, d_{\mathrm{f}})$ affecting the line between stations 1 and 3, with $R_{\mathrm{f}} \in \{0, 10, 20, 40, 80, 140\}\,\Omega$ and $d_{\mathrm{f}} \in \{2, 4, 6, 8, 10, 20, 30, 50, 80\}\,\mathrm{km}$. The fault distance d_{f} is taken with respect to station 3. For all of the 54 values of the parameter vector, a fault is always detected by the 6 relays of the grid which trigger the identification algorithms at different time instants. The results at relays R_{31} and R_{13} allow to evaluate the efficiency of the proposed algorithm to identify all kind of faults occurring on the protected link, especially its dependability. The outcomes at the 4 other relays are used to verify the selectivity of the algorithm, *i.e.*, its capability of rejecting the hypothesis that a fault occurred on their respective monitored line.

In Figure 16, the green area corresponds to faults identified by the proposed algorithms run at relays R_{31} (left)

and R_{13} (right) in line L_{13} with parameters estimated with a relative error below 50% of d_{f}^* , *i.e.*, $\left|\widehat{d}_{\mathrm{f}} - d_{\mathrm{f}}^*\right| < 0.5 d_{\mathrm{f}}^*$; the orange area corresponds to faults identified in line L_{13} with a larger relative estimation error; the red area indicates faults that were not identified in line L_{13}. This dependability analysis shows that the algorithm successfully identifies faults on the line in almost all studied cases (100% for R_{31}, 83% for R_{13}). Only faults occurring very close to the remote station with a rather high impedance are not properly identified.

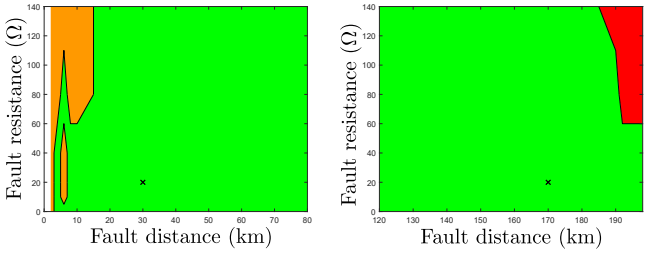

Figure 16: Results at relays R_{31} (left) and R_{13} (right): The green area corresponds to faults identified in line L_{13} with parameters estimated with a relative error below 50% of d_{f}^* , *i.e.*, $\left|\widehat{d}_{\mathrm{f}} - d_{\mathrm{f}}^*\right| < 0.5 d_{\mathrm{f}}^*$; the orange area corresponds to faults identified in line L_{13} with a larger relative estimation error; the red area indicates faults that were not identified in line L_{13}. Case 1, where $R_{\mathrm{f}}^* = 20\,\Omega$ and $d_{\mathrm{f}}^* = 30\,\mathrm{km}$, is indicated by a cross.

The duration of the measurement window required for the identification of all fault cases at relay R_{31} and R_{13} is showed in Figure 17. For all faults actually identified in line L_{13}, a measurement window of less than $200\,\mu\mathrm{s}$ is required. This confirms that the proposed algorithm is compatible with an ultra-fast fault clearing strategy.

The relative precision of the estimated distance for the different fault cases is summarized and compared with several state-of-the-art methods in the Table 6. The distance error is defined as a percentage of the total length of the line, $e_{\mathrm{d}} = \left(\widehat{d}_{\mathrm{f}} - d_{\mathrm{f}}^*\right)/d$. Though the precision of the proposed approach is lower, it is able to take the decision to trip the line using a measurement window 20 times smaller

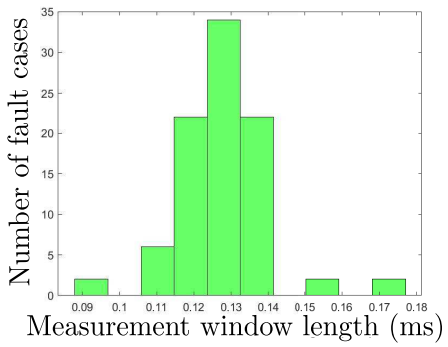

Figure 17: Duration of the observation window required for fault identification at relays R_{31} and R_{13}.

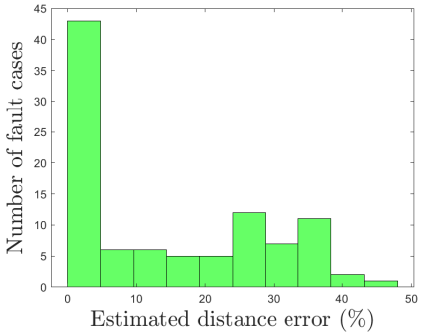

Figure 18: Relative error of the estimated fault distance at relays R_{31} and R_{13} for the extensive simulation fault cases.

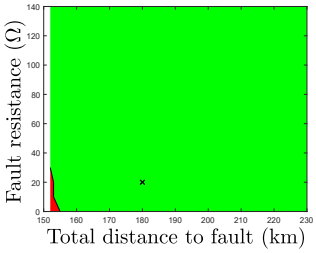

Figure 19: Results at relay R_{23}: The green area indicates faults that were correctly identified as external; The red area corresponds to faults that were incorrectly identified in the protected line L_{23}; Distance corresponds to the total distance between the fault and relay R_{23}; Case 1 with $R_{\mathrm{f}}^* = 20\,\Omega, d_{\mathrm{f}}^* = 180\,\mathrm{km}$ is indicated by a cross.

than the other methods. This makes it suitable as a primary fault identification algorithm for selective protection strategies. For the proposed approach the distribution of the error for the different fault cases is detailed in Figure 18. The relative error is less than 5% of the total line length for more 40 cases which represents about half of the fault cases identified on line L_{13}.

The selectivity analysis is presented for the relay R_{23} in Figure 19. Selectivity at the three other relays is ensured in all fault cases, due to the direction of the current wave which travels backwards. This is not the case for relay R_{23} and selectivity may be a challenge in some cases. This can be observed in Figure 12 where the area of the confidence ellipse evaluated at R_{23} goes much closer to the threshold compared to that evaluated at relays R_{21}, R_{12}, or R_{32}. The green area corresponds to faults that were correctly identified as outside the monitored line L_{23}. The red area corresponds to faults that were incorrectly identified in line L_{23}. Distances represent the total distance between the faults and relay R_{23}. The algorithm is selective for a wide range of fault cases. Few selectivity failures can be noticed for faults occurring very close to the relay R_{31} and having a low impedance. In such cases, the estimation algorithm wrongly identifies the fault in line L_{23} with a large fault distance and resistance.

In summary, the simulations show that the proposed approach has a satisfying behavior over a wide range of

Table 6: Comparison between the proposed scheme and other presented schemes.

Reference	Data window (ms)	Average error (%)	Tripping decision
[22]	13	0.02	No
[40]	10	0.3	No
[41]	10	0.4	Yes
[27]	5.3	2.3	Yes
Proposed algorithm	0.1	15	Yes
Proposed algorithm	0.3	12	Yes

fault cases affecting line L_{13}. Additional tests indicate similar behavior of the algorithm for faults occurring on the other lines. One possibility to handle dependability failures for remote faults is to use inter-tripping [42], since the remote relay (here R_{13}) will perform an ultra-fast fault identification.

8. Conclusion and future work

This paper proposes a novel single-ended algorithm for fault identification for meshed HVDC grids. Once a fault is suspected in a monitored line, the algorithm estimates the parameters of this fault using a combined physical and behavioral model to represent the fault propagation and to account for ground effects and various losses. A validity and an accuracy tests are then used to determine whether the monitored line is actually affected by a fault.

Taking full benefit of the information contained in the first waves after fault occurrence, identification of the fault can be performed observing the voltage and current at a relay during less than 200 μs. Contrary to existing single ended algorithm, DC reactors are not required to achieve selectivity. Extensive simulations with EMTP software showed that the method is applicable on a wide range of fault cases regarding fault distance and resistance.

Several future directions may be considered. The model has to be improved for faults lying close to a line end, since many reflections will be observed in such case. A possible solution to increase robustness regarding both selectivity and dependability is to run within the same relay several estimation algorithms with different initializations and to rely on a voting system among the provided estimates. Finally, an extension of the proposed algorithm to the multi-conductor case is still challenging.

Acknowledgment

This work was carried out at the SuperGrid Institute, an institute for the energetic transition (ITE). It is supported by the French government under the frame of "*Investissements d'avenir*" program with grant reference number ANE-ITE-002-01

Appendix A. Loss-less line approximation

For the physical part of the model in Section 4.1, the lines have been considered as lossless and with constant distributed parameters. The relevance of those approximations is illustrated here considering the line characteristics in Tables 2 and 4.

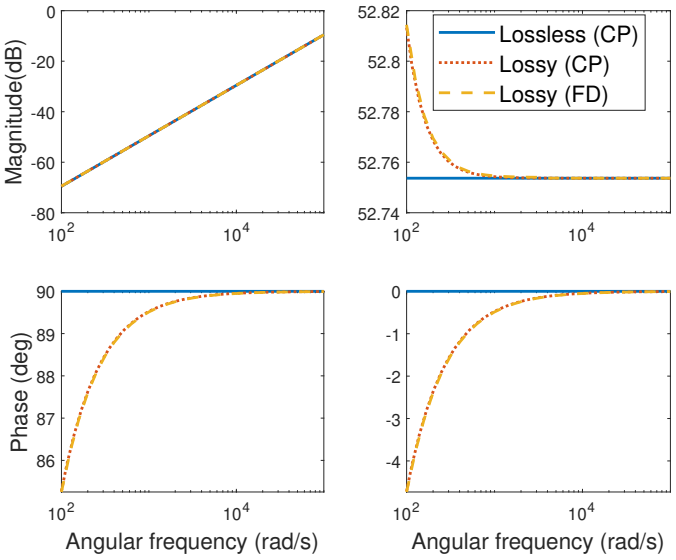

Figure A.20: Bode diagrams of the propagation constant γ (left) and of the characteristic impedance Z_c (right), lossless and lossy models with frequency dependent or constant line parameters.

Figure A.20 represents the evolution of the characteristic impedance $Z_c = \sqrt{Z/Y}$ and the propagation constant $\gamma = \sqrt{YZ}$ as a function of the frequency. We compared the general lossy case with frequency dependent (FD) line parameters, the lossy case with constant (frequency independent) line parameters (CP), and the proposed lossless approximation using constant parameters. Since the transient behavior has frequency content above 1 kHz, the lossless approximation is close to the general lossy case.

Appendix B. Non-blocking MMC stations

In Section 4.1.1 RLC equivalents have been considered to model the MMC stations, assuming the power electronic components within the stations are not blocked during the very first instants after the fault occurrence. To study the validity of this assumption, consider a single line connecting stations q and q' affected by a fault very close to station q. The rise of current at station q due to the multiple reflections between the station and the fault can be upper bounded by the rise of current in a worst case

scenario, where the fault is an ideal short-circuit and the station is an ideal voltage source. In that case each traveling wave reaching the station q will increase the current flowing through the MMC by a step of magnitude $2\frac{v_{\mathrm{bf}}}{Z_{\mathrm{c}}}$. Considering that the prior fault voltage is close to the nominal DC voltage V_{DC}, this step can be converted in per unit using the nominal DC power P_{DC} as,

$$2\frac{V_{\mathrm{DC}}^2}{Z_{\mathrm{c}}P_{\mathrm{DC}}}.$$

Thus, the per unit value of the current flowing through the MMC after 2 traveling waves is

$$1+4\frac{V_{\mathrm{DC}}^2}{Z_{\mathrm{c}}P_{\mathrm{DC}}},$$

again considering a worst case where the prior fault current in the line is 1p.u. For the parameters considered in Section 7.1 the current reaches 1.94p.u. The auto-blocking of the IGBTs within the MMC is generally considered to be active when the current reaches 2p.u. Hence, considering that the previous derivations are rather conservative, it is reasonable to model the 2 first waves assuming the MMC are not blocked.

References

[1] E. Pierri, O. Binder, N. G. Hemdan, M. Kurrat, Challenges and opportunities for a European HVDC grid, Renewable and Sustainable Energy Reviews 70 (2017) 427–456. doi:10.1016/j.rser.2016.11.233.

[2] P. Rodriguez, K. Rouzbehi, Multi-terminal DC grids: challenges and prospects, Journal of Modern Power Systems and Clean Energy 5 (4) (2017) 515–523. doi:10.1007/s40565-017-0305-0.

[3] WP4 PROMOTIoN, Report on the broad comparison of protection philosophies for the identified grid topologies, Tech. rep. (2018).

[4] CIGRE B4/B5.59, Protection and local control of HVDC-grids, Tech. rep., CIGRE (2018).

[5] D. Van Hertem, O. Gomis-Bellmunt, J. Liang, HVDC Grids For Offshore and Supergrid of the Future, Wiley-IEEE Press, 2016.

[6] K. Shinoda, A. Benchaib, J. Dai, X. Guillaud, Virtual Capacitor Control for Stability Improvement of HVDC System Comprising DC Reactors, in: Proc. Conference on AC and DC Power Transmission, 2019, pp. 1–6.

[7] WP6 PROMOTIoN, Develop system level model for hybrid DC CB, Tech. Rep. 691714 (2016).

[8] N. Johannesson, S. Norrga, Estimation of travelling wave arrival time in longitudinal differential protections for multi-terminal HVDC systems, Proc. 14th International Conference on Developments in Power System Protection (DPSP 2018) 2018 (15) (2018) 1007–1011. doi:10.1049/joe.2018.0225.

[9] D. Loume, A. Bertinato, B. Raison, B. Luscan, A multi-vendor protection strategy for HVDC grids based on low-speed DC circuit breakers, in: Proc. 13th IET International Conference on AC and DC Power Transmission (ACDC), Manchester, 2017, pp. 1–6. doi:10.1049/cp.2017.0008.

[10] Hermann W. Dommel, Digital Computer Solution of Electromagnetic Transients in Single-and Multiphase Networks, IEEE Transactions on Power Apparatus and Systems 88 (4) (1969) 388 – 399. doi:10.1109/TPAS.1969.292459.

[11] J. Mahseredjian, S. Dennetière, L. Dubé, B. Khodabakhchian, L. Gérin-Lajoie, On a new approach for the simulation of transients in power systems, Electric Power Systems Research 77 (11) (2007) 1514–1520.

[12] S. Le Blond, R. Bertho, D. V. Coury, J. C. Vieira, Design of protection schemes for multi-terminal HVDC systems, Renewable and Sustainable Energy Reviews 56 (2016) 965–974. doi:10.1016/j.rser.2015.12.025.

[13] B. Chang, O. Cwikowski, M. Barnes, R. Shuttleworth, A. Beddard, P. Coventry, Review of different fault detection methods and their impact on pre-emptive VSC-HVDC dc protection performance, High Voltage 2 (4) (2017) 211–219. doi:10.1049/hve.2017.0024.

[14] M. Ashouri, C. L. Bak, F. Faria Da Silva, A review of the protection algorithms for multi-terminal VCD-HVDC grids, in: Proc. IEEE International Conference on Industrial Technology (ICIT), 2018, pp. 1673–1678. doi:10.1109/ICIT.2018.8352433.

[15] W. Leterme, J. Beerten, D. Van Hertem, Non-unit protection of HVDC grids with inductive DC cable termination, IEEE Transactions on Power Delivery 31 (2) (2016) 820–828. doi:10.1109/TPWRD.2015.2422145.

[16] R. Li, L. Xu, L. Yao, DC fault detection and location in meshed multiterminal HVDC systems based on DC reactor voltage change rate, IEEE Transactions on Power Delivery 32 (3) (2017) 1516–1526. doi:10.1109/TPWRD.2016.2590501.

[17] S. Pirooz Azad, D. Van Hertem, A Fast Local Bus Current-Based Primary Relaying Algorithm for HVDC Grids, IEEE Transactions on Power Delivery 32 (1) (2017) 193–202. doi:10.1109/TPWRD.2016.2595323.

[18] A.-K. Marten, C. Troitzsch, D. Westermann, Non-telecommunication based DC line fault detection methodology for meshed HVDC grids, in: Proc. AC and DC Power Transmission (ACDC), Birmingham, 2015. doi:10.1049/iet-gtd.2015.0700.

[19] G. Auran, J. Descloux, S. Nguefeu, B. Raison, Non-unit full selective protection algorithm for MTDC grids, in: Proc. IEEE Power & Energy Society General Meeting, Chicago, 2017, pp. 1–5.

[20] C. Xi, Q. Chen, L. Wang, A single-terminal traveling wave fault location method for VSC-HVDC transmission lines based on S-transform, in: Proc. IEEE PES Asia-Pacific Power and Energy Engineering Conference (APPEEC), Xi'an, 2016, pp. 1008–1012. doi:10.1109/APPEEC.2016.7779647.

[21] A. Guzman-Casillas, B. Kasztenny, Y. Tong, M. V. Mynam, Accurate single-end fault locating using traveling-wave reflection information, in: Proc. Developments In Power System Protection, Belfast, 2018, pp. 1–6.

[22] J. Suonan, S. Gao, G. Song, Z. Jiao, X. Kang, A novel fault-location method for HVDC transmission lines, IEEE Transactions on Power Delivery 25 (2) (2010) 1203–1209. doi:10.1109/TPWRD.2009.2033078.

[23] Y. Liu, A. Sakis Meliopoulos, Z. Tan, L. Sun, R. Fan, Dynamic state estimation-based fault locating on transmission lines, IET Generation, Transmission & Distribution 11 (17) (2017) 4184–4192. doi:10.1049/iet-gtd.2017.0371.

[24] R. Razzaghi, G. Lugrin, H. Manesh, C. Romero, M. Paolone, F. Rachidi, An efficient method based on the electromagnetic time reversal to locate faults in power networks, IEEE Transactions on Power Delivery 28 (3) (2013) 1663–1673. doi:10.1109/TPWRD.2013.2251911.

[25] X. Jin, G. Song, Z. Ma, A Novel Pilot Protection for VSC-HVDC Transmission Lines Based on Parameter Identification, in: Proc. 12th IET International Conference on Developments in Power System Protection (DPSP), Vol. 05, Institution of Engineering and Technology, Copenhagen, 2014, pp. 1–6. doi:10.4236/epe.2013.54B224.

[26] N. Johannesson, S. Norrga, C. Wikström, Selective Wave-Front Based Protection Algorithm for MTDC Systems, in: Proc. 13th International Conference on Development in Power System Protection (DPSP), Edinburgh, 2016, pp. 1–6. doi:10.1049/cp.2016.0051.

[27] A. Ali Al Hage, B. Piepenbreier, D. Buchstaller, M. Engel, Multiple model based fault localization for HVDC transmission systems: Robustness and real-world performance, in: Proc. IEEE/PES Transmission and Distribution Conference and Exposition (T&D), Dallas, 2016, pp. 1–5. doi:10.1109/TDC.2016.7519987.

[28] M. Wang, J. Beerten, D. Van Hertem, Frequency domain based DC fault analysis for bipolar HVDC grids, Journal of Modern Power Systems and Clean Energy 5 (4) (2017) 548–559. doi:10.1007/s40565-017-0307-y.

[29] L. Bewley, Traveling Waves on Transmission Systems, Transactions of the American Institute of Electrical Engineers 50 (2) (1931) 532–550. doi:10.1109/ee.1942.6436308.

[30] G. Auran, Full selective protection strategy for multi-terminal cable HVDC grids based on HB-MMC converters, Phd thesis, Université Grenoble Alpes (2017). doi:10.1097/JGP.0b013e31819e2d50.

[31] W. Leterme, D. Van Hertem, Reduced Modular Multilevel Converter Model to Evaluate Fault Transients in DC Grids, in: Proc. 12th IET International Conference on Developments in Power System Protection (DPSP), 2014. doi:10.1049/cp.2014.0107.

[32] J. De Andrade Suárez, E. Sorrentino, Typical expected values of the fault resistance in power systems, in: Proc. IEEE/PES Transmission and Distribution Conference and Exposition: Latin America, Sao Paulo, 2010, pp. 602–609. doi:10.1109/TDC-LA.2010.5762944.

[33] A. Wasserrab, G. Balzer, The significance of frequency-dependent overhead lines for the calculation of HVDC line short-circuit currents, Electrical Engineering 97 (3) (2015) 213–223. doi:10.1007/s00202-014-0323-0.

[34] L. Ljung, System Identification - Theory for the User, Prentice-Hall, Englewood Cliffs, NJ, 1987.

[35] E. Walter, L. Pronzato, Identification of parametric models from experimental data, Springer-Verlag London, 1997.

[36] S. M. Kay, Fundamentals of Statistical Signal Processing: Estimation Theory, Prentice Hall PTR, 1993.

[37] A. Zama, S. Bacha, A. Benchaib, D. Frey, S. Silvant, A novel modular multilevel converter modelling technique based on semi-analytical models for HVDC application, Journal of Electrical Systems 12 (4) (2016) 649–659.

[38] O. R. Leanos, Wideband Line Cable Models for Realt Time and Off Line Simulations of ElectroMagnetic Transients, Phd thesis, Ecole Polytechnique de Montréal (2013).

[39] IEEE Substations Committee, IEEE Guide for Measuring Earth Resistivity, Ground Impedance, and Earth Surface Potentials of a Grounding System - Redline, Tech. rep. (2012). doi:10.1109/IEEESTD.2012.6392181.

[40] M. Farshad, J. Sadeh, A novel fault-location method for HVDC transmission lines based on similarity measure of voltage signals, IEEE Transactions on Power Delivery 28 (4) (2013) 2483–2490. doi:10.1109/TPWRD.2013.2272436.

[41] A. E. Abu-Elanien, A. A. Elserougi, A. S. Abdel-Khalik, A. M. Massoud, S. Ahmed, A differential protection technique for multi-terminal HVDC, Electric Power Systems Research 130 (2016) 78–88. doi:10.1016/j.epsr.2015.08.021.
URL http://dx.doi.org/10.1016/j.epsr.2015.08.021

[42] Network Protection & Automation Guide, Alstom Grid, 2011.